FISEVIER

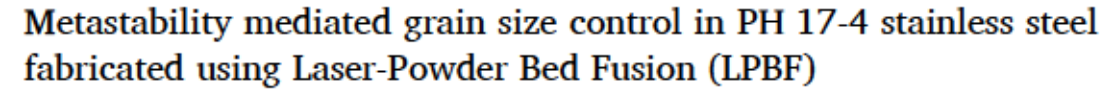
Contents lists available at ScienceDirect

Materialia

journal homepage: www.elsevier.com/locate/mtla



Full Length Article



Kaushalendra K Singh, Atieh Moridi

Sibley School of Mechanical and Aerospace Engineering, Cornell University, 124 Hoy Road, 469 Upson Hall, Ithaca, NY, 14853, USA



ARTICLE INFO

Keyword:
Additive manufacturing
Laser powder bed fusion
PH 17-4 stainless steel
Microstructure
Mechanical properties
heat treatment

ABSTRACT

Varying the chemical composition and cooling rates during additive manufacturing (AM) can enable the formation and, in some cases, the retention of metastable phases affecting the solidification pathways. Altering the solidification pathways directly affects the microstructure and in turn the mechanical properties of the parts. In this study, we show that modifying the solidification pathway through the deliberate retention of metastable austenite in PH 17–4 stainless steel (SS) leads to significant grain refinement (one order of magnitude smaller grains) and improvement in tensile strength (30% higher ultimate tensile strength) of parts printed using Laser-Powder Bed Fusion (LPBF). Nitrogen (N₂)-atomized feedstock powder containing higher concentrations of austenite-stabilizing elemental nitrogen was used to print parts with retained austenite. Parts absent of retained austenite printed using argon-atomized feedstock powder were used for comparison of microstructure and tensile properties. The grain refinement has been attributed to the "crowding effect" observed due to the simultaneous growth and coexistence of metastable austenitic phase with the stable ferrite. We also show that employing a three-step heat treatment procedure can eliminate the unwanted yield point behavior associated with the softer austenite while preserving the superior tensile properties in N2-atomized samples.

1. Introduction

Precipitation hardened Fe-17Cr-4Ni-4Cu steel or simply PH 17-4 stainless steel (SS), is one of the most commonly used martensitic steel which combines high strength with excellent corrosion resistance [1-3]. Owing to its excellent mechanical properties, PH 17-4 SS has widespread applications in the energy, defense, food storage and naval industries [4-10]. PH 17-4 SS is also widely used in the fabrication of injection molds [11-13] which require a combination of high strength and high wear resistance. When produced through conventional methods, PH 17-4 SS microstructure consists primarily of a body centered tetragonal (BCT) martensitic phase along with small quantities of the body centered cubic (BCC) &-ferrite phase. PH 17-4 SS is usually strengthened through an aging process via the formation of spherical Cu-rich precipitates [14-17].

With the rapid growth of the additive manufacturing (AM) industry and its promise to produce near-net-shape parts, there has been a growing interest in production of steels through AM [18-27]. The good printability of PH 17-4 SS along with its versatile application in many industries have made it one of the most popular steels in AM. In the case of AM PH 17-4 SS, a wide range of phase compositions have been reported for parts printed using powder bed fusion (PBF) [1,2,7-17]. Unlike conventionally manufactured PH 17-4 SS, PBF printed PH 17-4 SS can retain metastable austenite at room temperatures. Large variations in the volume fraction of retained austenite (0-97%) has been observed based on variations in process parameters, particularly the elemental composition of the feedstock powder [28,32-38]. Although the concentration of each alloying element is controlled based on standard specifications, slight variation within the specified limits is shown to have a significant impact on the microstructure of PBF printed parts. Even the type of shielding gas used during printing is shown to have altered the microstructure of PBF printed PH 17-4 SS [5,32]. The presence of retained austenite has shown to greatly affect the mechanical properties of the AM PH 17-4 SS. Based on the austenitic volume fraction, a wide range of strength-ductility combinations have been observed in AM PH17-4 SS [39-42]. The retained austenite's ability to easily transform into martensite upon deformation enhances the ductility of the printed part. The improved ductility, however, comes at the cost of reduced yield strength as the softer austenitic phase deforms at lower stress values. Owing to this poor yield strength, the retained

E-mail address: moridi@cornell.edu (A. Moridi).

^{*} Corresponding author.

austenite is often viewed as a deleterious phase and efforts are usually focused on preventing its retention during printing.

While the effect of retained austenite on the mechanical properties of PBF printed PH 17-4 SS has been studied extensively, the impact of the retained metastable phase on the microstructure of the as-deposited parts is not well-understood. This study aims to fill that gap by investigating the impact of retained austenite on the grain morphology in laser PBF printed PH 17-4 SS. Metastable austenite was deliberately retained through the use of N_2 -atomized feedstock powders while parts printed with powders atomized in Ar were used for comparison. Based on detailed metallographic characterization, we propose the solidification pathways and dynamics of grain growth in the two aforementioned samples. The tensile behavior of the as printed samples is investigated to understand the impact of different microstructures on the mechanical performance of printed parts. Moreover, we employ a standard threestep heat treatment procedure to eliminate the metastable austenite and further study the tensile behavior of the heat-treated samples.

2. Experimental

PH 17-4 powders atomized in argon and nitrogen atmospheres were procured from Carpenter Technology Corporations, UK. The elemental compositions of both feedstock powders are presented in Table 1. All samples were printed using a SLM280 Twin Laser machine with argon as the shielding gas. Both samples were printed with a 40 m layer thickness at a volumetric energy density of 66.7 J/mm³. The volumetric energy density (VED) was calculated using VED $P/(v \times d \times h)$ where P is the laser power, v is the laser scanning speed, d is thickness of the powder layer and h is the hatch spacing. The printed samples were sectioned and polished using a standard polishing procedure. Some polished samples were etched with Kalling s reagent to reveal the microstructures for observation by optical microscopy (OM). Microstructure, grain size, grain orientation and phase compositions were evaluated with a Tescan Mira field-emission scanning electron microscope (FE-SEM) via electron backscattering diffraction (EBSD) equipped with a QUANTAX EBSD apparatus. The EBSD data was analyzed using ATEX software [43]. The Scheil-Gulliver simulations were performed using the 'pycalphad-scheil package in the pycalhad toolbox [44,45]. To study the effect of heat treatment, some as-built samples from both Ar and N2 atomized conditions were exposed to a three-step heating process. The samples first undergo homogenization at 1176 C for 90 mins in vacuum, followed by a solution treatment at 1040 C for 60 mins with a subsequent final aging treatment at 551 C for 4 h. Tensile experiments were carried out on using a Deben MT2000 micro-tensile stage with a 2 kN load cell (Deben UK Ltd, Suffolk, UK) and digital image correlation (DIC) was used to capture the tensile strains. The error bars on the tensile data were calculated based on deviation from the mean value.

3. Results and discussion

3.1. Microstructure and phase composition

The OM images for the Ar- and N_2 -atomized samples parallel to the build direction are shown in Fig 1. Large columnar grains can be easily observed in the Ar-atomized samples whereas the grain shape isn t clearly resolved at the same magnification in the case of N_2 -atomized samples. Moreover, the grains in the Ar-atomized samples span across multiple melt pool boundaries showing the epitaxial nature of the grain growth. The formation of such columnar grains oriented along the build

direction is a direct consequence of the cyclic thermal history and the directional heat flow experienced during the laser PBF process [11]. Furthermore, different defect types were observed in the OM images of the two samples. The defect type observed throughout the Ar-atomized samples was gas porosities (encircled with solid red line) whereas larger lack of fusion (shown with dotted lines) defect was primarily observed at multiple locations in the N₂-atomized samples. Further microscopic characterization at higher magnifications using EBSD was conducted to study the morphology and orientation of the grains in the two samples.

The inverse pole figure (IPF) maps obtained from the EBSD analysis of both Ar and $\rm N_2$ atomized samples are shown in Fig 2. It is important to note here that the scale of the Ar-atomized samples is an order of magnitude higher than that of $\rm N_2$ -atomized counterpart. Similar to the OM images, large columnar grains oriented parallel to the build direction were observed in the Ar-atomized samples. The median size of the grains was estimated to be 10.40 $\,$ m with a standard deviation $\,$ 15.78 $\,$ m. The grain morphology observed in the $\rm N_2$ -atomized samples was strikingly different.

The N_2 -atomized samples show significant grain refinement with a median grain size of 0.74 m (standard deviation 0.80 m), which is one order of magnitude smaller than the grain size in the Ar-atomized case. Furthermore, the orientation of the grains in the N_2 -atomized samples is more random when compared to the highly oriented grains observed in the Ar-atomized samples. The multiples of uniform distribution (MUD) values obtained from the pole figures of specific planes was used to quantify and compare the crystallographic texture [46 48]. The pole figure for the (100) plane for both cases is plotted in Fig 2(c, d) and the corresponding MUD values confirm that the grains in the N_2 -atomized sample are oriented more randomly (max MUD 3.34) when compared to the highly textured grains in the Ar-atomized samples (max MUD 6.78).

The phase composition of printed samples atomized under different atomizing gases was markedly different. The phase maps indicate that the Ar-atomized samples consists primarily of a single BCC phase whereas a mixture of BCC and face centered cubic (FCC) phases were observed in the case of N_2 -atomized samples (Fig. 3). The observed FCC phase in the N_2 -atomized case can be assigned to the metastable austenitic () phase. The identification of the observed BCC phase, however, is more involved. The lattice parameters of the ferritic (BCC) phase and the martensitic (BCT) phase are very close to each other and EBSD alone cannot effectively distinguish between these two phases [4]. Consequently, the areas indexed as BCC can be either ferrite, martensite or a mixture of these two phases.

One method used to identify these phases involves the comparison of the grain misorientation using a Kernel average misorientation (KAM) map obtained from the EBSD data [29,30]. KAM quantifies the extent the local deformation at a point within the grain with respect to its nearest neighbors [49,50]. The martensitic phase in stainless steel is formed through a solid-state transformation of the metastable austenitic phase wherein the parent phase undergoes shape change as well as volumetric expansion. The deformation caused as a result of these structural changes show up as regions of high misorientations in the KAM maps [51,52]. The KAM maps with similar view fields for both cases are shown in Fig 4. The N2-atomized samples contains a mix of high and low misorientation regions spread throughout the sample confirming that both martensite and -ferrite are present in N2-atomized samples. In contrast, the regions of high misorientation in the Ar-atomized samples limited only to the high-angle grain boundaries which are expected to have higher misorientations. The absence of

Table 1 Chemical compositions of Ar and N₂ atomized PH 17-4 SS stainless steel powders (wt.%).

Powder	С	N	Mo	Cu	Nb	Ni	Cr	Si	Mn	Fe
Ar -atomized	0.02		0.01	3.31	0.28	4.38	15.76	0.41	0.39	balance
N ₂ -atomized	0.05	0.09	0.05	3.17	0.26	3.35	15.45	0.64	0.30	balance

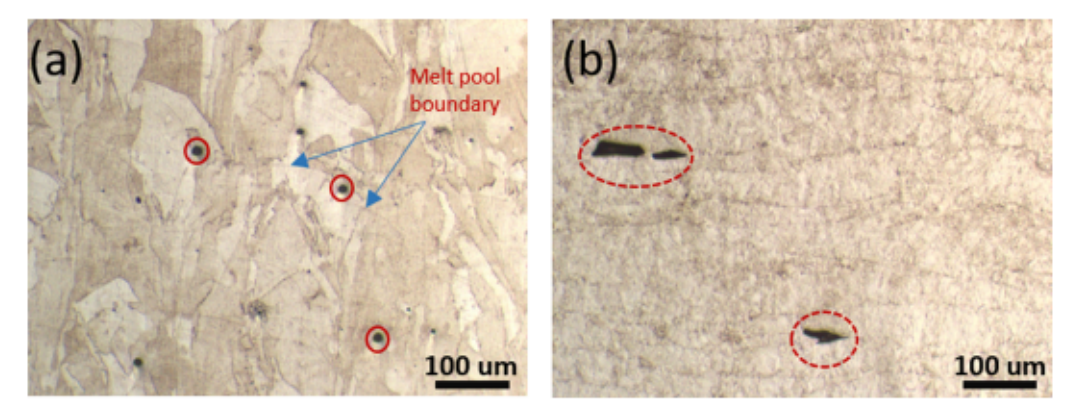


Fig. 1. OM images of (a) Ar-atomized and (b) N2-atomized samples.

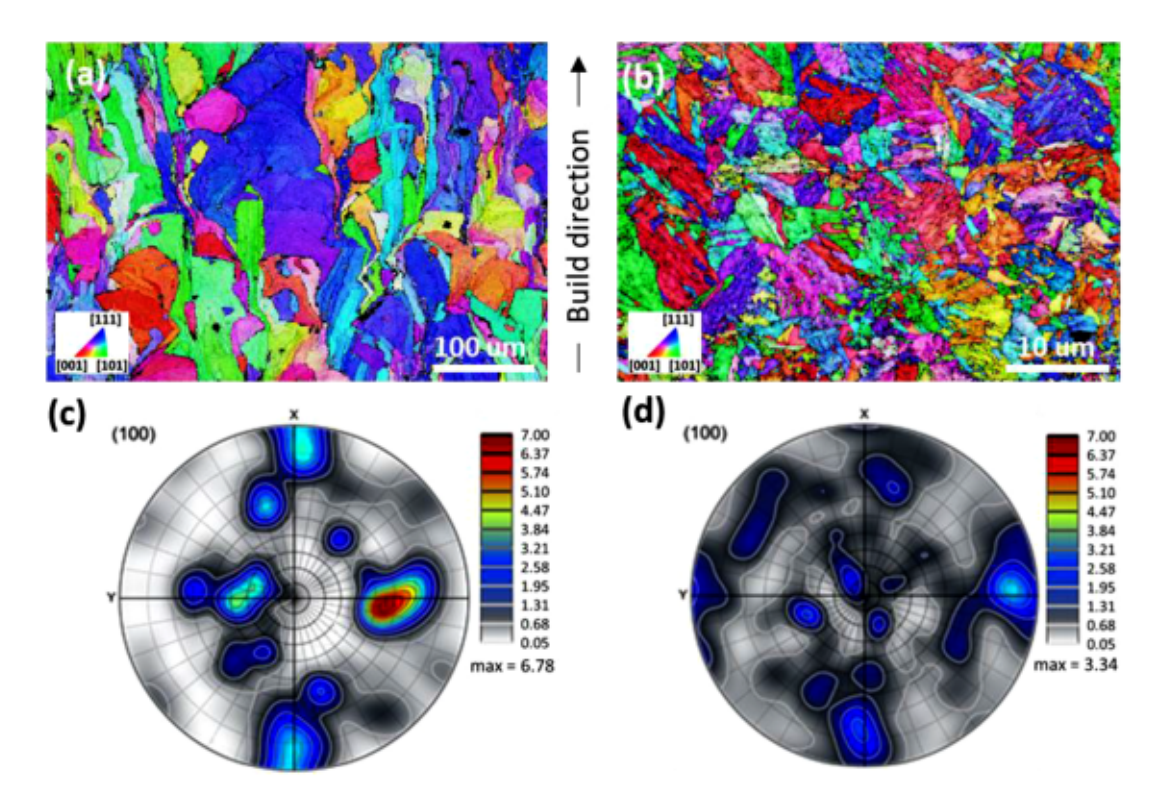


Fig. 2. IPF-Z maps parallel to the build direction and pole figures for the (100) plane shown for (a, c) Ar - and (b, d) N2 -atomized PH 17-4 SS samples.

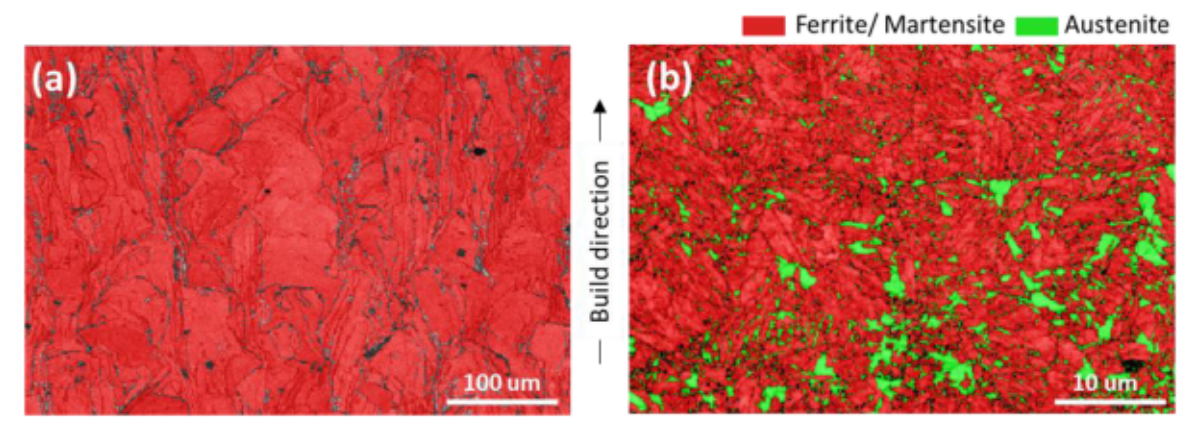


Fig. 3. Phase composition maps of as printed (a) Ar - and (b) N2 -atomized PH 17-4 SS printed samples.

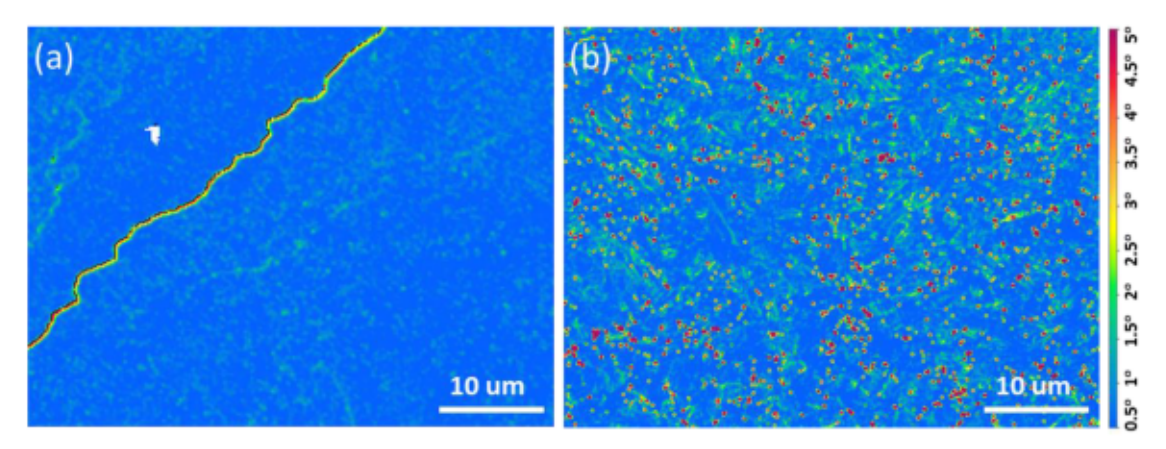


Fig. 4. KAM maps of as printed (a) Ar - and (b) N2 -atomized PH 17-4 SS printed samples. The color bar shows the degree of misorientation corresponding to each color

regions of high misorientation other than the grain boundaries in the Ar-atomized samples suggest that δ-ferrite is the majority phase.

The difference in the observed microstructures and the phase composition is a direct consequence of the combined effects of feedstock composition and different solidification pathways. The phase composition of PH 17-4 SS is strongly dependent on the elemental composition of the feedstock powder. Certain elements such as Ni, C, N and Mn [53-56] strongly stabilize the austenitic phase whereas other elements such Cr, Si, Nb and Mb favor the formation of the ferritic phase [57]. The composition of the solidified phase can be predicted using the Schaeffler's equivalent equations [58,59] which provide the relationship between different alloying elements to facilitate the calculation of the Chromium (Creq) and Nickel (Niea) equivalent values:

$$Cr_{eq} = [Cr] + [Mo] + 1.5 \times [Si] + 0.5 \times [Nb]$$

$$Ni_{eq} = [Ni] + 30 \times [C] + 30 \times [N] + 0.5 \times [Mn]$$

The Creo/Nieo ratio, calculated using the above equations, serves as a guide to predict the phase composition after solidification. The Crea/Niea ratio for the Ar-atomized powders was calculated to be 2.76 while that for the N2-atomized powders was 2.10. A higher Creq/Nieq value favors the formation of the ferrite phase whereas lower Creq/Nieq value enables the formation of the austenitic phase. In the context of this study, the use of N2 gas as the atomizing media instead of Ar resulted in an approximate 0.09% increase in the N concentration of the feedstock powder. The lower Creq/Nieq ratio in the case of N2-atomized powders suggests a higher possibility of austenite retention in the N2- atomized samples when compared to its Ar-atomized counterparts. The austenitic phase fraction was quantified with the help of a Scheil-Gulliver simulation tool based on pycalphad. The Scheil-Gulliver model has shown to be more accurate under non-equilibrium conditions, typically arising from the incomplete diffusion of alloying elements in the solid-state during solidification. The equivalent chromium and nickel values calculated using Schaeffler's equations were used as input composition for the Scheil simulations. These values served as a means for accounting the overall influence of all the constituent elements. The predicted solidification pathway for both sets of powders is very similar (Fig. 5). Upon cooling from the liquid phase, the δ-ferrite phase is expected to solidify first followed by the solidification of the austenitic phase at lower temperatures. The phase fraction of austenite in the case of N2-atomized powders (0.07) is, however, projected to be higher than the Ar-atomized case (0.01).

Even though these predictions match well with our experimental findings, the use of Scheil-Gulliver model for the prediction of phase composition of PBF printed parts is not completely accurate. In the case of metal AM, the Scheil-Gulliver model does not account for the changes in the phase composition caused as a result of the high cooling rates associated with powder bed fusion (105-107 K/s). Higher cooling rates can alter the solidification pathway and in turn modify the phase composition [21,31,60]. According to the equilibrium phase diagram for PH 17-4 SS, the solidification proceeds initially through the formation of δ-ferrite from the liquid phase. Next, the γ-austenite can either nucleate from the liquid or form through a solid-state transformation from δ -ferrite. Upon further cooling, the δ -ferrite transforms completely to the austenitic phase which in turn transforms to the stable martensitic phase when quenched. This solidification sequence, however, becomes inaccurate at high cooling rates. More specifically, the higher cooling rates lower the time available for the transformation of the δ -ferrite to

1760

1780

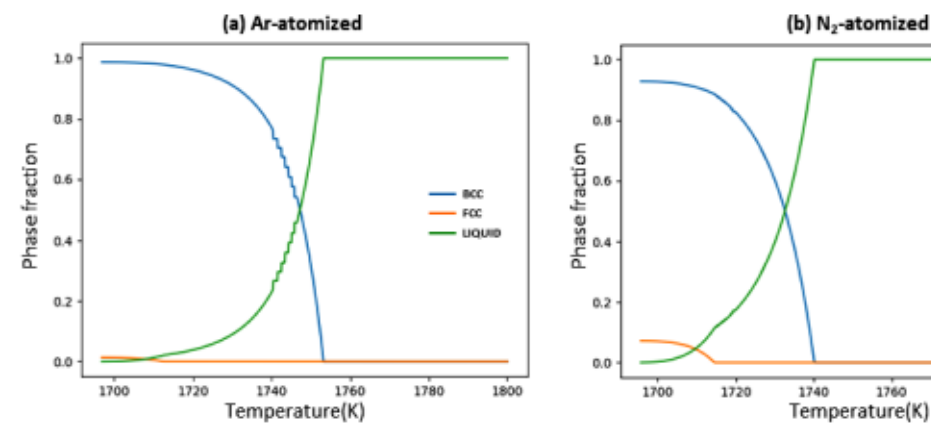


Fig. 5. The predicted phase fraction as a function of temperature(K) shown for (a) Ar-atomized and (b) N2-atomized PH 17-4 SS powders.

γ-austenite which is a diffusion-controlled process. The δ-ferrite effectively bypasses the austenite stability temperature range and exists as the thermodynamically stable BCC phase at room temperature without undergoing any further transformations.

This same phenomenon is observed in the case of the Ar-atomized samples. The δ-ferrite phase nucleates from the liquid but doesn't have enough time to transform to the austenite phase. At the relatively low concentration of nitrogen present in the Ar-atomized sample, δ-ferrite is the only phase to nucleate from the liquid. These ferritic grains continue to grow for a longer duration before they are impinged upon by another ferritic grain. This unrestricted growth results in the formation of large grains which further increase in size as they remelt and resolidify in response to the cyclic thermal history observed during laser PBF. The solidification pathway of the N2-atomized, however, is expectedly different. Unlike the Ar-atomized samples, the higher concentration of austenite stabilizing N in the N2-atomized feedstock enables the nucleation of the austenite phase alongside δ-ferrite. Upon solidification, both phases grow simultaneously from their respective nuclei, however their coexistence stops the grains from growing freely. We hypothesize that the coexistence of both ferritic and austenitic grains restricts the available space for a growing grain before it encounters another grain. We refer to this interaction between the ferrite and austenite grains as the "crowding effect". This crowding effect results in smaller grain sizes and explains the grain refinement observed in the N2atomized samples. Higher concentration of N also explains the presence of the metastable austenite at room temperatures. Thermodynamicsbased computations have shown that martensitic start temperature (Ms), which is the temperature at which the Gibbs free energy difference between the austenitic and martensitic phases reaches the critical driving force for martensitic nucleation, decreases with an increase in nitrogen content in stainless steel alloys [4,61]. At the higher N composition observed in the case of N2-atomized samples, the martensitic transformation initiates at a lower temperature. This leads to an incomplete transformation of austenite to martensite and results in the retention of metastable austenite at room temperature. Consequently, all three phases (δ-ferrite, austenite, and martensite) are observed in the N2-atomized samples. A schematic showing the solidification pathways for both atomizing conditions is shown in Fig. 6.

3.2. Mechanical properties

The mechanical behavior under tensile loading was also notably different for the Ar and N2 atomized samples. The stress-strain curves of the as-printed and the heat-treated samples for both atomizing conditions are shown in Fig. 7. The as-printed Ar-atomized samples showed continuous yielding wherein the stress increased initially till the point of ultimate tensile strength (UTS) and then decreased uniformly till failure. Contrarily, the tensile behavior of the as printed N2-atomized sample was not uniform as marked by the presence of yield point elongation (YPE) wherein the strain increased continuously at a constant stress value. This YPE is a consequence of the strain-induced transformation of the retained austenite to martensite. The deformation caused during tensile loading leads to the formation of nucleation sites favorable for the transformation of the metastable austenite to the energetically favorable martensitic phase. The strain-induced transformation of the retained austenite to martensite acts as an additional deformation mode and results in strain hardening [62,63]. This phenomenon is similar to the martensitic transformation observed in transformation induced

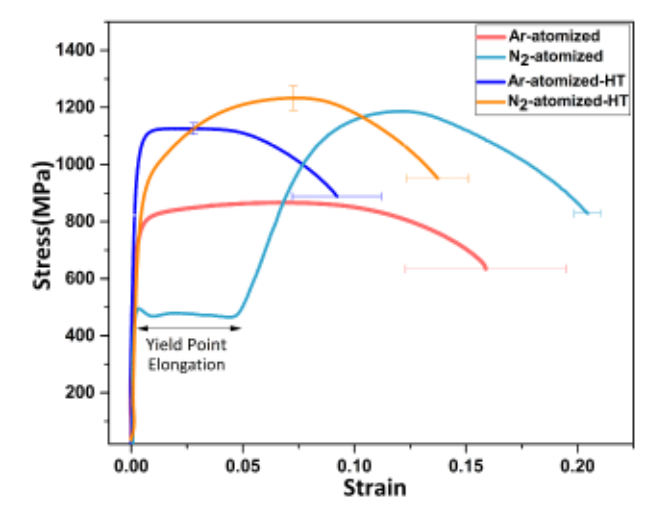


Fig. 7. Stress strain curves for the as-printed and heat-treated samples for both samples.

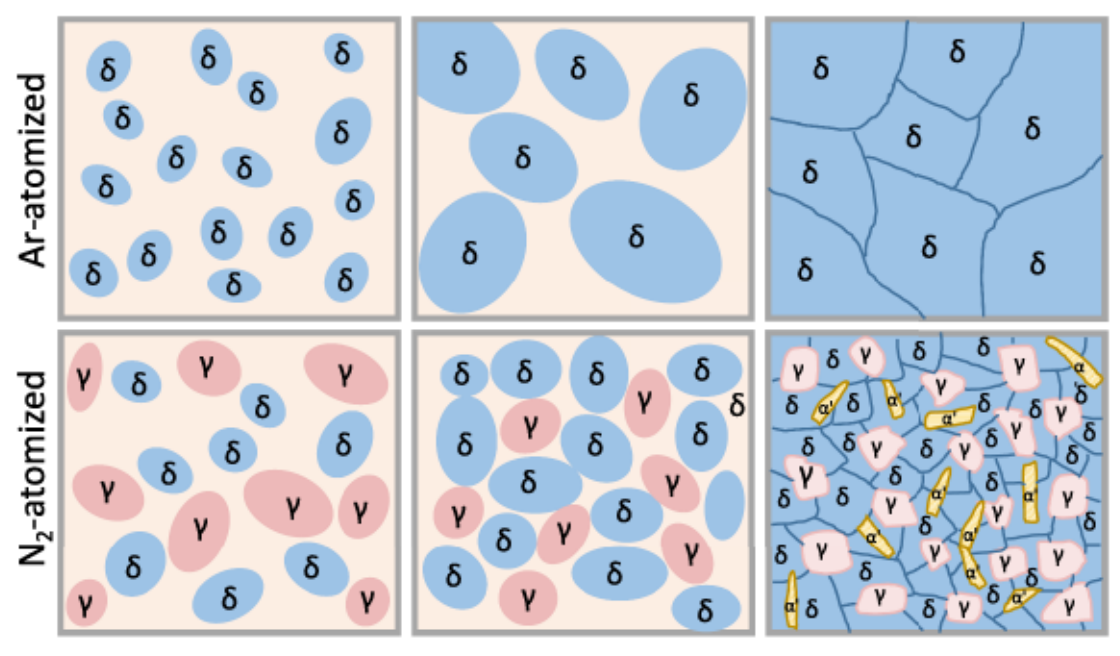


Fig. 6. Schematic of solidification pathway and grain growth.

plasticity(TRIP) steels [64–66]. As a result of the smaller grain size and the presence of the harder martensitic phase, the UTS for the as printed N₂-atomized sample 1186 (± 35) MPa was expectedly higher than the Ar-atomized samples 866 (± 2) MPa. Interestingly though, the yield strength of the N₂-atomized samples was lower when compared to the Ar-atomized counterparts. The lower yield strength observed in N₂-atomized samples can be attributed to load partitioning, a well-known phenomenon often observed in duplex stainless steels [67, 68]. The austenitic phase is significantly softer than the martensitic/ferritic phase and accommodates most of the initial plastic deformation. As the strain increases, the load gradually transfers to the harder ferrite/martensite phase, resulting in improved tensile strength.

Owing to the YPE, the elongation at failure (EF) for the as printed N2atomized samples was also larger than the as printed Ar-atomized counterpart. However, the presence of YPE is detrimental for parts in service as they can undergo significant plastic deformation well below their UTS. Therefore, it is imperative to eliminate this YPE and improve the part's resistance to plastic deformation. To achieve this, we employed a three-step heat treatment process with the intention of eliminating YPE while preserving the superior mechanical properties of the N2-atomized samples. As seen in Fig. 7, the heat treated N2-atomized samples show a more continuous yielding behavior when compared to the as-printed N2-atomized samples. No regions showing increasing strain at constant stress values were observed confirming that YPE was successfully eliminated. EBSD analysis was performed on the heattreated samples to study microstructural changes when compared to the as-printed samples. The IPFZ maps of both heat-treated samples show lath-like structures typical of martensite (Fig. 8a, d). High misorientation regions in the KAM maps corresponding to the lathshaped grains confirm the presence of martensite (Fig. 8c, f). The phase maps (Fig. 8b, e) of the Ar-atomized sample comprise only of BCC/BCT phases, however, tiny fractions of austenitic phase still remain in the N2-atomized samples. Heat treatment has a similar effect on the mechanical properties of both samples wherein the UTS increases while the ductility decreases. Interestingly though, the UTS and ductility for the heat-treated N₂-atomized sample is still higher when compared to the Ar-atomized heat-treated counterparts. The yield stress for the heat-treated samples is also comparable in contrast to the as-printed samples wherein the N₂-atomized samples yielded at a much lower value. These findings provide a novel pathway to produce PBF printed PH 17-4 SS with improved mechanical properties using metastable austenite as an intermediary.

4. Conclusion

The effect of metastable retained austenite on the microstructure, phase composition and mechanical properties of PBF printed PH 17-4 SS samples has been investigated. Detailed characterizations of PBF printed parts with feedstock powders atomized using two different gases, Ar and N2 show strikingly different microstructures. The Ar-atomized sample was characterized by the presence of large columnar grains oriented parallel to the build direction. In the absence of austenite stabilizing N and at the high cooling rates associated with PBF process, the solidification bypasses the austenite stability temperature range and δ -ferrite is the only phase observed at room temperature. Interestingly, the grain morphology and phase composition of the N2-atomized sample printed under similar conditions was very different. The N2-atomized samples was composed of a mixture of δ-ferrite, metastable austenite and the martensitic phase. The presence of these phases enable refinement of the grain structure and improves the UTS of the printed sample albeit at the cost of introducing YPE and lowering the yield stress. However, with the implementation of an appropriate heat treatment procedure, the detrimental effects of YPE can be eliminated to get a final part with superior mechanical properties. It is important to highlight that the scope of the methodology mentioned in this study extends beyond PH 17-4 SS to other material systems wherein the microstructure and properties of AM

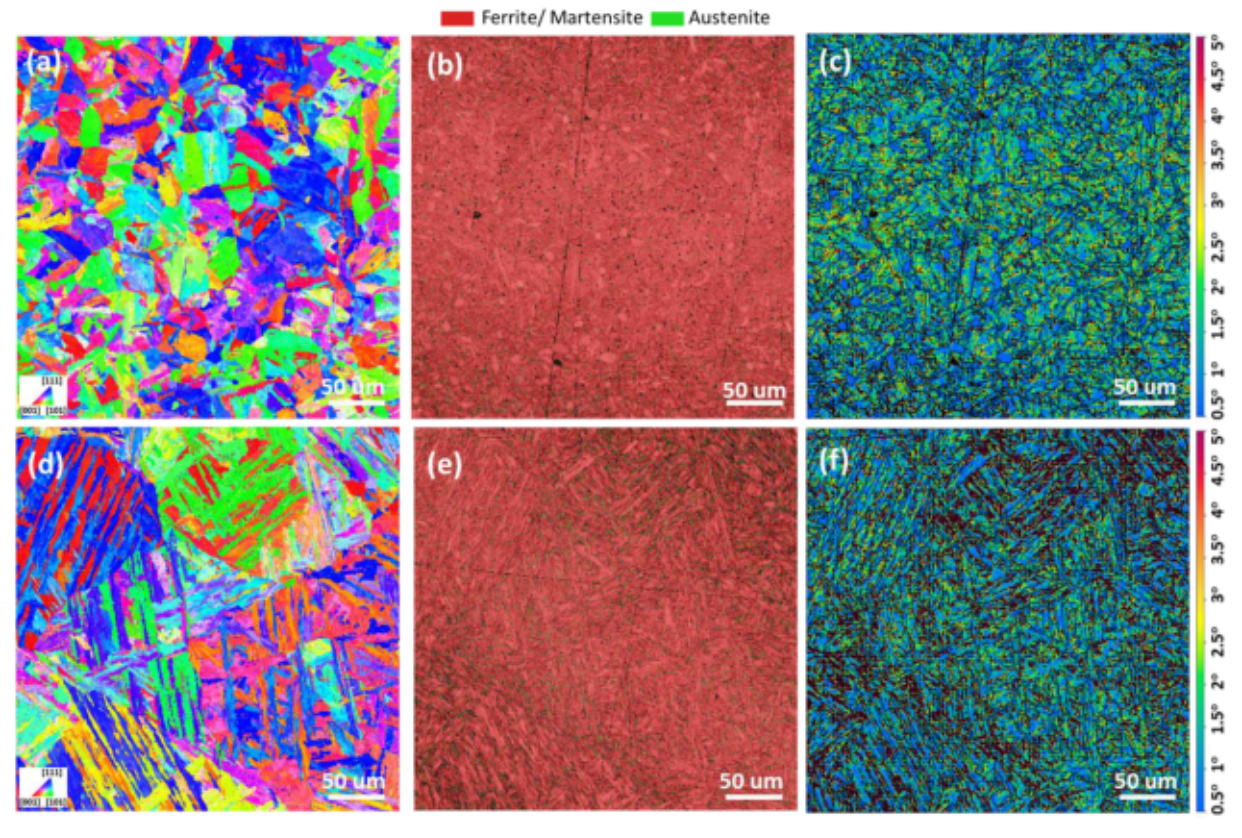


Fig. 8. IPF-Z, phase composition and KAM maps shown in (a,b,c) for heat-treated Ar-atomized and (d,e,f) for heat-treated N2-atomized sample.

parts can be tuned using metastable phases as an intermediary.

Data and materials availability

The datasets generated during and/or analyzed during the current study are available from the corresponding author on reasonable request.

CRediT authorship contribution statement

Kaushalendra K Singh: Investigation, Writing review & editing, Methodology, Data curation. **Atieh Moridi:** Conceptualization, Writing review & editing.

Declaration of Competing Interest

The authors declare that they have no known competing financial interests or personal relationships that could have appeared to influence the work reported in this paper.

Acknowledgments

Research supported by the by the U.S. department of Energy (DOE), office of science, basic energy science (BES) early career award # DE-SC0022860 (solidification pathway) and National Science Foundation (NSF) early career award #CMMI-2046523 and Office of Naval Research Young Investigator award # N00014-22-1-2420 (mechanical behavior). This work made use of the Cornell Center for Materials Research Shared Facilities which are supported through the NSF MRSEC program (DMR-1719875). Authors also acknowledge Moog Inc. for supplying the powders and printing the samples.

References

- J.-H. Wu, C.-K. Lin, Tensile and fatigue properties of 17-4 PH stainless steel at high temperatures, Metall. Mater. Trans. 33 (2002) 1715 1724, https://doi.org/ 10.1007/s11661-002-0180-8.
- [2] C.S. Carter, D.G. Farwick, A.M. Ross, J.M. Uchida, Stress corrosion properties of high strength precipitation hardening stainless steels, Corrosion 27 (1971) 190 197, https://doi.org/10.5006/0010-9312-27.5.190.
- [3] H.J. Rack, D. Kalish, The strength, fracture toughness, and low cycle fatigue behavior of 17-4 PH stainless steel, Metall. Trans. 5 (1974) 1595 1605, https:// doi.org/10.1007/BF02646331.
- [4] A. Baghdadchi, V.A. Hosseini, L. Karlsson, Identification and quantification of martensite in ferritic-austenitic stainless steels and welds, J. Mater. Res. Technol. 15 (2021) 3610 3621, https://doi.org/10.1016/J.JMRT.2021.09.153.
- [5] L.E. Murr, E. Martinez, J. Hernandez, S. Collins, K.N. Amato, S.M. Gaytan, P. W. Shindo, Microstructures and properties of 17-4 PH stainless steel fabricated by selective laser melting, J. Mater. Res. Technol. 1 (2012) 167 177, https://doi.org/10.1016/\$2238-7854(12)70029-7.
- [6] P. Bajaj, A. Hariharan, A. Kini, P. Kürnsteiner, D. Raabe, E.A. Jägle, Steels in additive manufacturing: a review of their microstructure and properties, Mater. Sci. Eng. A. 772 (2020), 138633, https://doi.org/10.1016/J.MSEA.2019.138633.
- [7] Y. Sun, R.J. Hebert, M. Aindow, Effect of heat treatments on microstructural evolution of additively manufactured and wrought 17-4PH stainless steel, Mater. Des. 156 (2018) 429 440, https://doi.org/10.1016/J.MATDES.2018.07.015.
- [8] C.F. Arisoy, G. Başman, M.K. Şeşen, Failure of a 17-4 PH stainless steel sailboat propeller shaft, Eng. Fail. Anal. 10 (2003) 711 717, https://doi.org/10.1016/ S1350-6307(03)00041-4.
- [9] W.T. Chien, C.S. Tsai, The investigation on the prediction of tool wear and the determination of optimum cutting conditions in machining 17-4PH stainless steel, J. Mater. Process. Technol. 140 (2003) 340–345, https://doi.org/10.1016/S0924-0136(03)00753-2.
- [10] S.V. Raj, L.J. Ghosn, B.A. Lerch, M. Hebsur, L.M. Cosgriff, J. Fedor, Mechanical properties of 17-4PH stainless steel foam panels, Mater. Sci. Eng. A. 456 (2007) 305 316, https://doi.org/10.1016/J.MSEA.2006.11.142.
- [11] H.L. Wei, J. Mazumder, T. Debroy, Evolution of solidification texture during additive manufacturing OPEN, Nat. Publ. Gr. (2015), https://doi.org/10.1038/ srep16446.
- [12] M.-W. Wu, Z.-K. Huang, C.-F. Tseng, K.-S. Hwang, Microstructures, mechanical properties, and fracture behaviors of metal-injection molded 17-4PH stainless steel, Met. Mater. Int. 21 (2015) 531 537, https://doi.org/10.1007/s12540-015-4369-y.
- [13] Y. Li, L. Li, K.A. Khalil, Effect of powder loading on metal injection molding stainless steels, J. Mater. Process. Technol. 183 (2007) 432 439, https://doi.org/ 10.1016/J.JMATPROTEC.2006.10.039.

- [14] U.K. Viswanathan, S. Banerjee, R. Krishnan, Effects of aging on the microstructure of 17-4 PH stainless steel, Mater. Sci. Eng. A. 104 (1988) 181 189, https://doi.org/ 10.1016/0025-5416(88)00420-X
- [15] C.N. Hsiao, C.S. Chiou, J.R. Yang, Aging reactions in a 17-4 PH stainless steel, Mater. Chem. Phys. 74 (2002) 134 142, https://doi.org/10.1016/S0254-0584(01) 00460-6
- [16] M. Murayama, Y. Katayama, K. Hono, Microstructural evolution in a 17-4 PH stainless steel after aging at 400 C, Metall. Mater. Trans. A Phys. Metall. Mater. Sci. 30 (1999) 345 353, https://doi.org/10.1007/S11661-999-0323-2/METRICS.
- [17] W. Do Yoo, J.H. Lee, K.T. Youn, Y.M. Rhyim, Study on the microstructure and mechanical properties of 17-4 PH stainless steel depending on heat treatment and aging time, Solid State Phenom. 118 (2006) 15 20, https://doi.org/10.4028/ WWW SCIENTIFIC NET/SSP 118 15
- [18] M. Ma, Z. Wang, X. Zeng, A comparison on metallurgical behaviors of 316 L stainless steel by selective laser melting and laser cladding deposition, Mater. Sci. Eng. A. 685 (2017) 265 273, https://doi.org/10.1016/J.MSEA.2016.12.112.
- [19] B. Zhang, L. Dembinski, C. Coddet, The study of the laser parameters and environment variables effect on mechanical properties of high compact parts elaborated by selective laser melting 316 L powder, Mater. Sci. Eng. A. 584 (2013) 21 31, https://doi.org/10.1016/J.MSEA.2013.06.055.
- [20] Q.B. Nguyen, Z. Zhu, F.L. Ng, B.W. Chua, S.M.L. Nai, J. Wei, High mechanical strengths and ductility of stainless steel 304 L fabricated using selective laser melting, J. Mater. Sci. Technol. 35 (2019) 388–394, https://doi.org/10.1016/J. JMST.2018.10.013.
- [21] E. Johnson, L. Gråbæk, A. Johansen, L.S. Kristensen, J.V. Wood, Microstructure of rapidly solidified stainless steel, Mater. Sci. Eng. 98 (1988) 301–303, https://doi. org/10.1016/0025-5416(88)90174-7.
- [22] K. Abd-Elghany, D.L. Bourell, Property evaluation of 304 L stainless steel fabricated by selective laser melting, Rapid Prototyp. J. 18 (2012) 420 428, https://doi.org/ 10.1108/13552541211250418/FULL/PDF.
- [23] S. Pasebani, M. Ghayoor, S. Badwe, H. Irrinki, S.V. Atre, Effects of atomizing media and post processing on mechanical properties of 17-4 PH stainless steel manufactured via selective laser melting, Addit. Manuf. 22 (2018) 127 137, https://doi.org/10.1016/J.ADDMA.2018.05.011.
- [24] F. Hengsbach, P. Koppa, K. Duschik, M.J. Holzweissig, M. Burns, J. Nellesen, W. Tillmann, T. Tröster, K.P. Hoyer, M. Schaper, Duplex stainless steel fabricated by selective laser melting - microstructural and mechanical properties, Mater. Des. 133 (2017) 136 142, https://doi.org/10.1016/J.MATDES.2017.07.046.
- [25] K. Davidson, S. Singamneni, Selective laser melting of duplex stainless steel powders: an investigation, Mater. Manuf. Process. 31 (2016) 1543 1555, https://doi.org/10.1080/10426914.2015.1090605.
- [26] K.P. Davidson, S.B. Singamneni, Metallographic evaluation of duplex stainless steel powders processed by selective laser melting, Rapid Prototyp. J. 23 (2017) 1146 1163, https://doi.org/10.1108/RPJ-04-2016-0053.
- [27] K. Saeidi, L. Kevetkova, F. Lofaj, Z. Shen, Novel ferritic stainless steel formed by laser melting from duplex stainless steel powder with advanced mechanical properties and high ductility, Mater. Sci. Eng. A. 665 (2016) 59 65, https://doi. org/10.1016/J.MSEA.2016.04.027
- [28] T. LeBrun, T. Nakamoto, K. Horikawa, H. Kobayashi, Effect of retained austenite on subsequent thermal processing and resultant mechanical properties of selective laser melted 17-4 PH stainless steel, Mater. Des. 81 (2015) 44 53, https://doi.org/ 10.1016/J.MATDES.2015.05.026.
- [29] S. Sabooni, A. Chabok, S.C. Feng, H. Blaauw, T.C. Pijper, H.J. Yang, Y.T. Pei, Laser powder bed fusion of 17-4 PH stainless steel: a comparative study on the effect of heat treatment on the microstructure evolution and mechanical properties, Addit. Manuf. 46 (2021), 102176, https://doi.org/10.1016/J.ADDMA.2021.102176.
- [30] S.M. Yeon, J. Yoon, T.B. Kim, S.H. Lee, T.S. Jun, Y. Son, K. Choi, Normalizing effect of heat treatment processing on 17-4 PH stainless steel manufactured by powder bed fusion, Metals 12 (2022) 704, https://doi.org/10.3390/MET12050704.
- [31] S.A. David, J.M. Vitek, R.W. Reed, T.L. Hebble, Effect of rapid solidification on stainless steel weld metal microstructures and its implications on the Schaeffler diagram, (1987). https://doi.org/10.2172/5957599.
- [32] P.D. Nezhadfar, K. Anderson-Wedge, S.R. Daniewicz, N. Phan, S. Shao, N. Shamsaei, Improved high cycle fatigue performance of additively manufactured 17-4 PH stainless steel via in-process refining micro-/defect-structure, Addit. Manuf. 36 (2020), 101604, https://doi.org/10.1016/J.ADDMA.2020.101604.
- [33] A. Yadollahi, N. Shamsaei, S.M. Thompson, A. Elwany, L. Bian, Effects of building orientation and heat treatment on fatigue behavior of selective laser melted 17-4 PH stainless steel, Int. J. Fatigue. 94 (2017) 218 235, https://doi.org/10.1016/J. LIFATIGUE.2016.03.014.
- [34] B. AlMangour, J.M. Yang, Understanding the deformation behavior of 17-4 precipitate hardenable stainless steel produced by direct metal laser sintering using micropillar compression and TEM, Int. J. Adv. Manuf. Technol. 90 (2016) 119 126, https://doi.org/10.1007/S00170-016-9367-9.
- [35] E.A. Lass, M.R. Stoudt, M.E. Williams, Additively manufactured nitrogen-atomized 17-4 PH stainless steel with mechanical properties comparable to wrought, Metall. Mater. Trans. A Phys. Metall. Mater. Sci. 50 (2019) 1619 1624, https://doi.org/ 10.1007/S11661-019-05124-0/FIGURES/3.
- [36] L. Facchini, N. Vicente, I. Lonardelli, E. Magalini, P. Robotti, M. Alberto, Metastable austenite in 17-4 precipitation-hardening stainless steel produced by selective laser melting, Adv. Eng. Mater. 12 (2010) 184 188, https://doi.org/ 10.1002/ADEM.200900259.
- [37] D.J. Shaffer, A.E. Wilson-Heid, J.S. Keist, A.M. Beese, T.A. Palmer, Impact of retained austenite on the aging response of additively manufactured 17-4 PH grade stainless steel, Mater. Sci. Eng. A. 817 (2021), 141363, https://doi.org/10.1016/J. MSEA.2021.141363.

- [38] S.D. Meredith, J.S. Zuback, J.S. Keist, T.A. Palmer, Impact of composition on the heat treatment response of additively manufactured 17-4 PH grade stainless steel, Mater. Sci. Eng. A. 738 (2018) 44 56, https://doi.org/10.1016/J. MSFA 2018 09 066
- [39] L. Carneiro, B. Jalalahmadi, A. Ashtekar, Y. Jiang, Cyclic deformation and fatigue behavior of additively manufactured 17-4 PH stainless steel, Int. J. Fatigue. 123 (2019) 22 30, https://doi.org/10.1016/J.IJFATIGUE.2019.02.006.
- [40] N. Haghdadi, M. Laleh, M. Moyle, S. Primig, Additive manufacturing of steels: a review of achievements and challenges, J. Mater. Sci. 56 (2021) 64 107, https://doi.org/10.1007/S10853-020-05109-0/FIGURES/19.
- [41] P.D. Nezhadfar, R. Shrestha, N. Phan, N. Shamsaei, Fatigue behavior of additively manufactured 17-4 PH stainless steel: synergistic effects of surface roughness and heat treatment, Int. J. Fatigue 124 (2019) 188 204, https://doi.org/10.1016/J. LIFATIGUE.2019.02.039.
- [42] M. Mahmoudi, A. Elwany, A. Yadollahi, S.M. Thompson, L. Bian, N. Shamsaei, Mechanical properties and microstructural characterization of selective laser melted 17-4 PH stainless steel, Rapid Prototyp. J. 23 (2017) 280 294, https://doi. org/10.1108/RPJ-12-2015-0192/FUIL/XML.
- [43] J.-J. Fundenberger, B. Beausir, Analysis Tools for Electron and X-Ray Diffraction, ATEX-Software, Université de Lorraine - Metz, 2017. www.atex-software.eu.
- [44] R. Otis, Z.-K. Liu, pycalphad: CALPHAD-based computational thermodynamics in python, J. Open Res. Softw. 5 (2017) 1, https://doi.org/10.5334/JORS.140.
- [45] B. Bocklund, L.D. Bobbio, R.A. Otis, A.M. Beese, Z.-K. Liu, pycalphad-scheil: 0.1.6 (version 0.1.6), (2020). https://doi.org/http://doi.org/10.5281/zenodo.3630600.
- [46] R.J. Moat, A.J. Pinkerton, L. Li, P.J. Withers, M. Preuss, Crystallographic texture and microstructure of pulsed diode laser-deposited Waspaloy, Acta Mater. 57 (2009) 1220 1229, https://doi.org/10.1016/J.ACTAMAT.2008.11.004.
- [47] O. Gokcekaya, T. Ishimoto, T. Todo, P. Wang, T. Nakano, Influence of powder characteristics on densification via crystallographic texture formation: pure tungsten prepared by laser powder bed fusion, Addit. Manuf. Lett. 1 (2021), 100016, https://doi.org/10.1016/J.ADDLET.2021.100016.
- [48] F. Geiger, K. Kunze, T. Etter, Tailoring the texture of IN738LC processed by selective laser melting (SLM) by specific scanning strategies, Mater. Sci. Eng. A. 661 (2016) 240 246, https://doi.org/10.1016/J.MSEA.2016.03.036.
- [49] M. Kamaya, A.J. Wilkinson, J.M. Titchmarsh, Quantification of plastic strain of stainless steel and nickel alloy by electron backscatter diffraction, Acta Mater. 54 (2006) 539 548, https://doi.org/10.1016/J.ACTAMAT.2005.08.046.
- [50] M. Kamaya, Assessment of local deformation using EBSD: quantification of local damage at grain boundaries, Mater. Charact. 66 (2012) 56 67, https://doi.org/ 10.1016/J.MATCHAR.2012.02.001.
- [51] K.D. Zilnyk, D.R. Almeida Junior, H.R.Z. Sandim, P.R. Rios, D. Raabe, Misorientation distribution between martensite and austenite in Fe-31 wt%Ni-0.01 wt%C, Acta Mater. 143 (2018) 227 236, https://doi.org/10.1016/J. ACTAMAT.2017.10.026.
- [52] V. Atreya, C. Bos, M.J. Santofimia, Understanding ferrite deformation caused by austenite to martensite transformation in dual phase steels, Scr. Mater. 202 (2021), 114032. https://doi.org/10.1016/J.SCRIPTAMAT.2021.114032.

- [53] V. Raghavan, Effect of manganese on the stability of austenite in Fe-Cr-Ni alloys, Metall. Mater. Trans. A 26 (1995) 237 242, https://doi.org/10.1007/ BF02664662
- [54] Q. Wang, B. Zhang, K. Yang, Thermodynamic calculation study on effect of manganese on stability of austenite in high nitrogen stainless steels, Metall. Mater. Trans. A Phys. Metall. Mater. Sci. 47 (2016) 3284 3288, https://doi.org/10.1007/ s11661.016.3532.5
- [55] J. Speer, D.K. Matlock, B.C. De Cooman, J.G. Schroth, Carbon partitioning into austenite after martensite transformation, Acta Mater. 51 (2003) 2611 2622, https://doi.org/10.1016/S1359-6454(03)00059-4.
- [56] K. Kim, S.J. Lee, Effect of Ni addition on the mechanical behavior of quenching and partitioning (Q&P) steel, Mater. Sci. Eng. A 698 (2017) 183 190, https://doi.org/ 10.1016/J.MSFA.2017.05.030
- [57] S. Sirohi, C. Pandey, A. Goyal, Brief study on -ferrite characterization: a review, Mater. Today Proc. 50 (2022) 1367 1371, https://doi.org/10.1016/J. MATPR.2021.08.280.
- [58] A.L. Schaeffler, Constitution diagram for stainless steel weld metal, Met. Prog. (1949), 680–60B.
- [59] J. Ning, J.H. Wen, L.J. Zhang, S.J. Na, Assessment of the universality of duplex stainless steel powder in laser additive repair based on Schaeffler diagram, Addit. Manuf. 55 (2022), 102864, https://doi.org/10.1016/J.ADDMA.2022.102864.
- [60] J.W. Elmer, S.M. Allen, T.W. Eagar, The influence of cooling rate on the ferrite content of stainless steel alloys, (1989). https://doi.org/10.2172/5678406.
- [61] E.A. Lass, F. Zhang, C.E. Campbell, Nitrogen effects in additively manufactured martensitic stainless steels: conventional thermal processing and comparison with wrought, Metall. Mater. Trans. A Phys. Metall. Mater. Sci. 51 (2020) 2318 2332, https://doi.org/10.1007/s11661-020-05703-6.
- [62] J. Chiang, B. Lawrence, J.D. Boyd, A.K. Pilkey, Effect of microstructure on retained austenite stability and work hardening of TRIP steels, Mater. Sci. Eng. A 528 (2011) 4516 4521, https://doi.org/10.1016/j.msea.2011.02.032.
- [63] B.L. Ennis, E. Jimenez-melero, E.H. Atzema, M. Krugla, Metastable austenite driven work-hardening behaviour in a TRIP-assisted dual phase steel, Int. J. Plast. 88 (2017) 126 139, https://doi.org/10.1016/j.ijplas.2016.10.005.
- [64] W. Bleck, X. Guo, Y. Ma, The TRIP effect and its application in cold formable sheet steels, Steel Res. Int. 88 (2017), https://doi.org/10.1002/SRIN.201700218.
- [65] F.D. Fischer, G. Reisner, E. Werner, K. Tanaka, G. Cailletaud, T. Antretter, A new view on transformation induced plasticity (TRIP), Int. J. Plast. 16 (2000) 723 748, https://doi.org/10.1016/S0749-6419(99)00078-9.
- [66] M. Soleimani, A. Kalhor, H. Mirzadeh, Transformation-induced plasticity (TRIP) in advanced steels: a review, Mater. Sci. Eng. A 795 (2020), 140023, https://doi.org/ 10.1016/J.MSEA.2020.140023.
- [67] N. Haghdadi, C. Ledermueller, H. Chen, Z. Chen, Q. Liu, X. Li, G. Rohrer, X. Liao, S. Ringer, S. Primig, Evolution of microstructure and mechanical properties in 2205 duplex stainless steels during additive manufacturing and heat treatment, Mater. Sci. Eng. A (2022) 835, https://doi.org/10.1016/j.msea.2022.142695.
- [68] N. Haghdadi, P. Cizek, P.D. Hodgson, H. Beladi, Microstructure dependence of impact toughness in duplex stainless steels, Mater. Sci. Eng. A 745 (2019) 369–378, https://doi.org/10.1016/j.msea.2018.12.117.